Impedance-Based Harmonic Instability Assessment in a Multiple Electric Trains and Traction Network Interaction System

Tao, Haidong; Hu, Haitao; Wang, Xiongfei; Blaabjerg, Frede; He, Zhengyou

Published in:
I E E E Transactions on Industry Applications

DOI (link to publication from Publisher):
10.1109/TIA.2018.2793843

Publication date:
2018

Document Version
Accepted author manuscript, peer reviewed version

This article has been accepted for publication in a future issue of this journal, but has not been fully edited. Content may change prior to final publication. Citation information: DOI 10.1109/TIA.2018.2793843, IEEE Transactions on Industry Applications

Impedance-Based Harmonic Instability Assessment in Multiple Electric Trains and Traction Network Interaction System

Haidong Tao, *Student Member*, *IEEE*, Haitao Hu, *Member*, *IEEE*, Xiongfei Wang, *Senior Member*, *IEEE*, Frede Blaabjerg, *Fellow*, *IEEE*, Zhengyou He, *Senior Member*, *IEEE*

***Abstract*—This paper presents an impedance-based method to systematically investigate the interaction between multiple trains and traction network, focusing on evaluating the harmonic instability problem. Firstly, the interaction mechanism of multi-train and traction network is represented as a feedback interconnection of the two subsystems, i.e., an equivalent output impedance of the traction network and an equivalent input admittance of the multi-train. Then the harmonic instability is evaluated through a series of pole-zero diagrams drawn from the closed loop transfer matrix of the multi-train and network system (MTNS). The interaction system is unstable and the harmonic instability will happen if there are some high frequency poles of the closed loop system locating in the right half plane. This method is used for analyzing the harmonic instability phenomena, the characteristics, influential factors and potential mitigation schemes. The theoretical results are further validated by the simulations and experiments.**

***Index Terms*—electrified railways, harmonic instability, impedance-based analysis, multi-train and network interaction.**

I. INTRODUCTION

A. Motivations

BY the end of January 2017, the total mileage of the China high-speed railway (HSR) has exceeded 22 thousand kilometers, accounting for more than 60% in the world. It is vital to ensure the security and reliability of such a large scale transportation system. However, the current, voltage and phase-locked loop controllers of the high-speed trains (HSTs) may interact with each other and these controllers can further interact with the traction network, resulting in gradual amplification and instability in harmonic voltage and current of the traction network. This phenomenon has been named harmonic instability in [1-4].

These harmonic instability problems have been reported in China HSR lines:

1) The amplification phenomenon of the 47th to 55th harmonic current components occurred on the China HSR line in 2011. It led the control system of the HSTs to be unstable, the lightning arrestors of the HST to be burned, circuit breaker to be tripped and many other malfunctions to be happened.

2) The high-frequency harmonic voltage was amplified gradually on the China HSR line during February 23rd to 24th in 2011, which made the control system of the HSTs unstable, voltage and current seriously distorted and four arrestors even exploded.

3) The harmonic current rose on the China HSR line in 2015 as well as caused the current transformer to be exploded and also the traction substation to be tripped.

Overall, the harmonic instability has restricted the development of China HSR. Additionally, the harmonic instability phenomenon in railway was first reported in Zürich, Switzerland in 1995 [1] and the same to high voltage direct current systems (HVDC) [2], wind generation [3] and solar power generation [4].

The standard EN50388-2012 [5] described and classified the overvoltage problems occurred in the AC or DC electrified railways as system instability and harmonic problems. The harmonic instability problems in the electrified railways are caused by the interaction between the four-quadrant converter (4QC) of HST and network. However, the specific cases or in-depth modeling analysis are not given in this standard.

Based on the previous works, the input admittance of multi-train is usually equivalent to *n* times of a single HST [6-8]. This method is effective for analyzing the low frequency oscillation problem caused by a large number of HSTs gaining access to the traction network at the same rail depot. However, the harmonic instability in electrified railway system usually occurs during the normal operation modes. The HSTs at different catenary positions are coupled with each other due to the network impedance. Therefore, the equivalent modeling method is not suitable for analyzing the harmonic instability in the MTNS.

With the rapid development of the HSR, the harmonic instability resulted from the interaction between multi-train and traction networks caught more attention. The MTNS is a multiple input multiple output (MIMO) system, there is coupling among multiple HSTs, as well as multiple HSTs and traction network, which makes it more difficult to determine the occurrence conditions and stability margin of harmonic instability. The harmonic instability in the MTNS has not been addressed yet.

B. Literature Review

In order to identify the harmonic instability, the mainstream analysis methods can be classified into the following three categories: the nonlinear method [9], the state-space modeling

This work was supported by National Natural Science Foundation of China (NSFC 51677154, 51525702).

H. Tao, H. Hu and Z. He are with the School of Electrical Engineering, Southwest Jiaotong University, Chengdu, Sichuan, 610031, P.R. China (e-mail: thdswjtu@163.com, hht@swjtu.edu.cn, hezy@swjtu.edu.cn).

X. Wang and F. Blaabjerg are with the Department of Energy Technology Aalborg University, Aalborg 9220, Denmark (Email: xwa@et.aau.dk, fbl@et.aau.dk).

method [10], and the impedance-based method [11]. The nonlinear method has computational complexity and is difficult to study the large power electronics based power systems [12]. The state-space method needs to build state matrix of the interaction system and determine the oscillation mode based on eigenvalues and feature vectors of state matrix [10,13]. However, it is hard to establish detailed load model and dynamic network model with high switching frequency of the 4QC. In addition, adding or removing a source or a load, or changing the operation mode of a load need to re-establish the state matrix.

The impedance-based method has several advantages [14]: 1) A system impedance model and stability can be readily obtained and evaluated; 2) Changing the system structure and the source or load parameters only affect the impedance characteristics, hence the new system stability can be well assessed; 3) Impedance-based analysis can readily indicate possible solutions as well as damping design when a stability problem has been identified; 4) The impedance of the source or the load can be obtained through experiment or numerical simulation even when the system is a black box. Since the position of HST in the electrified railway is time-varying, the traction network structure and impedance will also be changed accordingly. Therefore, the impedance-based method is suitable for analyzing the stability of the interaction system between HST and network [5,6,8].

Currently, the impedance-based method is widely used for analyzing the stability of dynamical interconnected systems between the source (traction network) and the load (HST), such as wind and photovoltaic system [15], flexible HVDC system [16], railway system [6], DC microgrids [17], ship and aircraft power supply system [18] and so on. Based on the impedance analysis, there are following several criterions: impedance ratio criteria [19], positive-net-damping criteria [20], input-admittance criteria [21] and maximum peak criteria [22]. These methods are only suitable for a single input single output (SISO) system. For a MIMO system, the GNC [23] and the pole-zero of the closed loop transfer function [6] are the main methods for evaluating the system stability.

C. Contributions

The aim of this paper is to investigate the harmonic instability characteristics of the MTNS in frequency domain based on pole-zero theory, which can predict and describe the harmonic instability phenomenon. The contributions of this paper are:

1) The impedance models of the MTNS, including: a) the impedance model of the HST in *dq* frame combining the voltage controller, the current controller and the phase-locked loop, see Section III; b) the impedance model of multiple trains which are coupled due to the traction network impedance, see Section IV.

2) In Section V, the methodology and the impact of variable parameters (e.g., the current controller, the voltage controller, the phase locked loop and traction network parameters) on the harmonic instability in the MTNS are fully investigated.

3) In Section VI, both simulation and experimental results have been conducted to validate the proposed method, which helps to improve the interactive performance between multi-train and traction network as well as mitigate the newly-found harmful electrical issues, see Section VII.

II. Measured Analysis

Fig. 1 shows the total harmonic distortion of the traction network voltage (U_{THD}) under different HSR lines. The basic test conditions are as follows:

- *Test signals*: 1) the catenary voltage in Qionghai section post of a HSR line. 2) the catenary voltage in South Handan traction substation of a HSR line.
- *Test Methods*: the sampling interval is 2 seconds and the recording time is a continuous 24 hours.
- *Sampling frequency*: 50 kHz, that is, each sampling period is 1000 points.
- U_{THD} *range*: the harmonic voltage of 2nd-100th.

In Fig. 1(a), U_{THD} is suddenly amplified and rapidly decreased in a short time. As mentioned in [24], Fig. 1(a) is a typical harmonic resonance phenomenon. However, in Fig. 1(b), it can be seen that the U_{THD} and the 61st harmonic component are gradually amplified in a certain time and the peak of the harmonic voltage appears at about 15:00. This phenomenon is different from the harmonic resonance in Fig. 1(a).

Fig. 2 depicts two typical voltage waveforms corresponding to Fig. 1(b). Fig. 2(a) is the voltage waveform whose U_{THD} is approximately 5%, corresponding to about 10:00 in Fig. 1(b). Fig. 2(b) is the voltage waveform whose U_{THD} is approximately 20%, corresponding to about 15:00. It can be seen that the harmonic components of the centenary voltage will be gradually amplified, which may make the onboard control system unstable, causes overvoltage problems with capacitive devices and arresters. As mentioned in [1], this phenomenon indicates the harmonic instability problem.

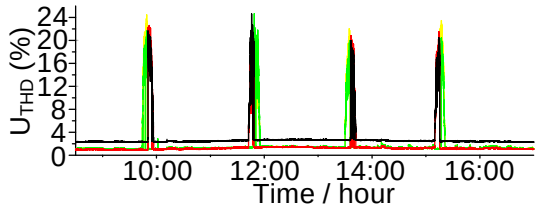

(a)

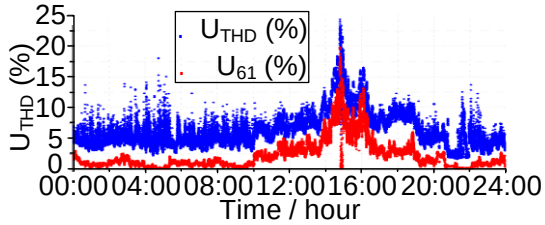

(b)

Fig. 1. Field test: (a) U_{THD} in Qionghai section post of a HSR line, China. (b) U_{THD} (blue) and the 61st harmonic component (red) in South Handan traction substation of a HSR line, China.

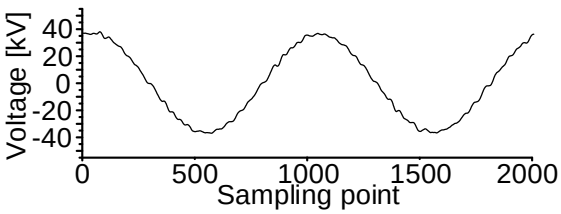

This article has been accepted for publication in a future issue of this journal, but has not been fully edited. Content may change prior to final publication. Citation information: DOI 10.1109/TIA.2018.2793843, IEEE Transactions on Industry Applications

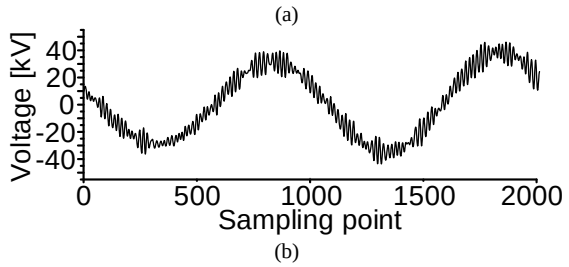

Fig. 2. Voltage waveform in South Handan traction substation of a HSR line: (a) The U_{THD} is approximately 5%; (b) The U_{THD} is approximately 20%.

III. Impedance Model and Analysis of a Single HST and Network System

The CRH5-type HST is one of the mainstream electrified trains in China HSR. Some controller modules, parameters and tuning principles have been introduced in [8]. The HST model can be divided into several parts according to its main circuit and controller structure. Meanwhile, for a nonlinear system, to permit stability analysis, linearization for small-signal perturbation quantities is needed. Then the analytical model of the impedance for the HST is performed along with the models of these parts together.

A. Main Circuit and Its DQ-Domain Admittance Model of the HST

The control block diagram of the HST is shown in Fig. 3. The control system includes the current controller (CC), voltage controller (VC) and phase-locked loop (PLL). L_{in} and R_{in} are the equivalent leakage inductance and resistance of the traction transformer, respectively. L_s and R_s are the equivalent inductance and resistance of the traction network, respectively. e_s is output voltage of the traction substation.

Notice that being different from the *abc*/*αβ* transformation of the three phase ac system, a second-order generalized integrator (SOGI) is usually used to transform the instantaneous value of measured single phase ac voltages and currents into a rotating reference framework (*αβ* quadrature signal). Therefore, there are two synchronous rotating frames, i.e., network *dq* frame and 4QC *dq* frame. The error angle $\Delta\theta = \theta - \theta_0$ must be taken into account if there are some fluctuations around the steady-state point. In this paper, the superscript *c* is adopted for distinguishing the 4QC *dq* frame from the network *dq* frame.

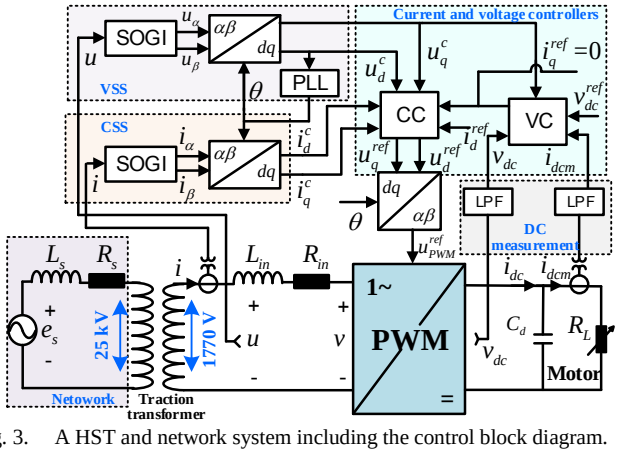

Fig. 3. A HST and network system including the control block diagram.

The analytical transfer functions derivation of the PLL, CC and VC are presented in Appendix A. The HST and network interaction system shown in Fig. 3 is split between the traction network and the HST subsystem. The input admittance of the HST can be given by

$$\Delta\mathbf{I}(s) = \left[\mathbf{G}_{CC}\mathbf{G}_{VC} + \mathbf{Y}_{CC}\mathbf{G}_{uPLL} + \mathbf{G}_{iPLL}\right]\Delta\mathbf{U}(s)$$
$$\Rightarrow \Delta\mathbf{I}(s) = \underbrace{\begin{bmatrix} Y_{dd} & Y_{dq} \\ Y_{qd} & Y_{qq} \end{bmatrix}}_{\mathbf{Y}_{train}(s)}\Delta\mathbf{U}(s) \quad (1)$$

where $\mathbf{G}_{uPLL}(s)$ and $\mathbf{G}_{iPLL}(s)$ represent the voltage and current transfer functions of the PLL, respectively. $\mathbf{Y}_{CC}(s)$ and $\mathbf{G}_{CC}(s)$ are the input admittance and transfer function of the CC, respectively. $\mathbf{G}_{VC}(s)$ represents the transfer function of the VC.

Fig. 4 depicts the impedance frequency responses of the HST where the simulation parameters in Appendix B are used. It can be seen that the negative damping in the low frequency domain of *dd* channel will be generated by the VC. In addition, the VC has empty impact on the impedance of *qq* channel. Similarly, the PLL only affects the impedance characteristics of the *qq* channel and *qd* channel since the synchronization feature of the PLL. For a rectifier, the positive damping characteristic in the low frequency domain of *qq* channel will be exhibited. In contrast, for an inverter, the negative damping characteristic in the low frequency domain will be obtained [23,25].

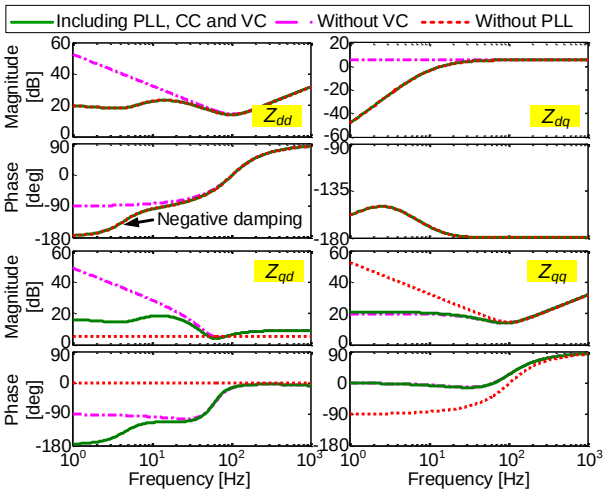

Fig. 4. Impedance frequency responses of the HST with different controllers. The green solid line denotes the impedance frequency responses of the HST including CC, VC and PLL. The pink chain dotted line and red dotted line denote the impedance frequency responses which only including CC, PLL and CC, VC, respectively.

B. Impedance Model of the Traction Network

The electrified railway traction system can be divided into ac and dc solutions. The dc traction system is mainly used in France, Japan (dc 11.5 kV) and Italy (dc 3 kV). The ac traction power supply system is widely used in the world, which has 15 kV / 16.67Hz [8], 25kV / 60Hz [26] and 25 kV / 50Hz modes. In addition, the 25 kV traction power system includes the 1×25 kV, (for the directly fed traction network, respect to the conventional railway) [27], and 2×25 kV, (for the AT-fed traction network, respect to the high-speed or overloaded railway),

which are mainly used in Korea [26], Italy [28], Europe [29], China [30-32], Iran [33] and Zimbabwe [34].

The AT-fed catenary system is generally adopted in China HSR. The mathematical model of the traction network mainly contains the equivalent circuit model, generalized symmetrical component model, and chain-circuit model [35]. The equivalent circuit model with resistance-inductance is widely used for tuning the control of inverters and studying the control performance [8,10]. For a single-phase ac system, the active and reactive power of the traction network can be considered as a *dq* system. From [6], the network impedance is transmitted as

$$\begin{bmatrix}\Delta u_d\\ \Delta u_q\end{bmatrix}=\underbrace{\begin{bmatrix}R_s+sL_s & -\omega_0 L_s\\ \omega_0 L_s & R_s+sL_s\end{bmatrix}}_{\mathbf{Z}_s(s)}\begin{bmatrix}\Delta i_d\\ \Delta i_q\end{bmatrix} \tag{2}$$

where Δ denotes the small deviation of the respective variable from the equilibrium point. Compared with the input voltage $\mathbf{U}(s)$ of the HST, the output voltage $\mathbf{E}_s(s)$ of the traction substation has a higher voltage value due to the onboard traction transformer as shown in Fig. 3. In addition, the input admittance of the HST in Fig. 3 is only determined by the 4QC. Each HST has five same power units and those power units in a single train are all in parallel. Since each power unit is regarded as two same 4QC in parallel. Therefore, the minor-loop gain can be expressed as

$$\begin{aligned}\mathbf{L}&=[10\cdot\mathbf{Y}_{train}(s)]\frac{\mathbf{Z}_s(s)}{k^2}=\mathbf{Y}_{train}(s)\left[\frac{10\cdot\mathbf{Z}_s(s)}{k^2}\right]\\&=\mathbf{Y}_{train}(s)\mathbf{Z}_s^*(s)\end{aligned} \tag{3}$$

where k is the ratio of transformer.

C. Stability Analysis of A Single HST and Network System

In this subsection, the impact of the network inductance (L_{01}^*) and the proportional gain of CC (Kp_{CC}) on the stability of a single HST and network system will been investigated by the generalized Nyquist criteria (GNC). The simulation parameters in Appendix B are used. Fig. 5 shows the impedance frequency responses of the HST and the network impedance. The red and blue solid lines denote the impedance of the network and HST, respectively. It can be seen that the diagonal elements of the network and HST have no interaction under the initial parameters. When increasing the L_{01}^* or Kp_{CC} (see the red and blue dotted line, respectively), the diagonal elements of the network and HST intersect with each other and the network impedance is inductive and the HST impedance is capacitive in *dd* channel. This phenomenon indicates that there is a risk of instability.

The minor-loop gain $\mathbf{Y}_{train}(s)\mathbf{Z}_s^*(s)$ in (3) is taken into consideration and the GNC is applied to evaluate the stability. The stability conditions of the initial values (i.e., Case 1) can be predicted correctly as shown in Fig. 6(a). When the Kp_{CC} is 15 (i.e., Case 2) or L_{01}^* is 20 mH (i.e., Case 3), the characteristic locus (λ_2) in Fig. 6 will encircle the critical point (-1, j0), which means the system is unstable.

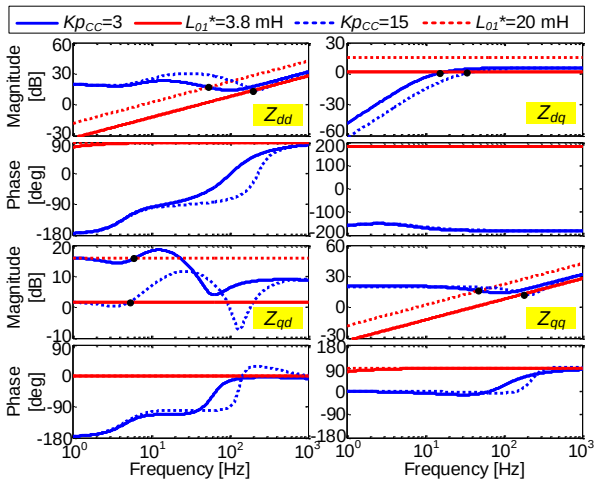

Fig. 5. Impedance frequency responses of the HST and traction network for different Kp_{CC} and L_{01}^*.

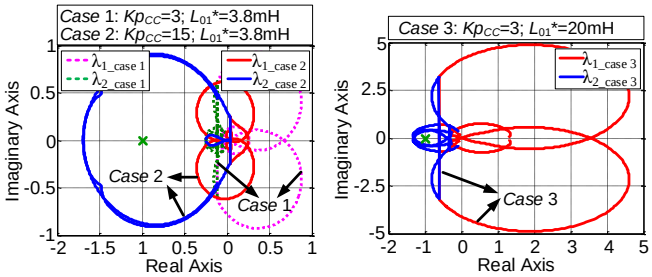

Fig. 6. Generalized Nyquist contours of (a) Case 1 and Case 2; (b) Case 3.

IV. Impedance Model and Analysis of the MTNS

Different from the stability issues of a single HST system, the multi-train at different catenary positions are connected to the network impedance, as shown in Fig. 7. Therefore, an equivalent model of the HST with *n* times larger network cannot be applied. A impedance-based model is proposed to solve this problem.

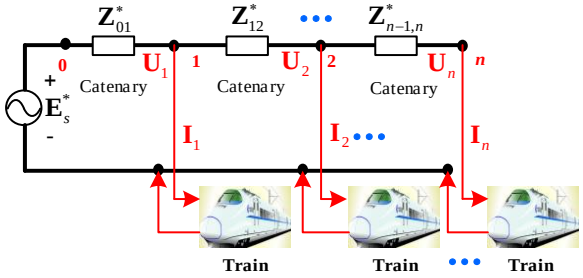

Fig. 7. A typical configuration of the MTNS.

A. Impedance Model of the MTNS

The MTNS in Fig.7 is a multivariable system, in which the input and output vectors are the input voltages and currents of each HST. The *i*-th node demonstrates the position of the *i*-th HST connected to the network, $\mathbf{Z}_{ij}^*(s)$ (with *i*, *j*=1,2,…,*n*; *i*≠*j*) represent the network impedance between node *i* and node *j*, $\mathbf{U}_i(s)$ and $\mathbf{I}_i(s)$ (with *i*=1,2,…,*n*) are the input voltage and the input current of the *i*-th HST, respectively. Applying the Kirchhoff law in Fig.7, one can obtain

This article has been accepted for publication in a future issue of this journal, but has not been fully edited. Content may change prior to final publication. Citation information: DOI 10.1109/TIA.2018.2793843, IEEE Transactions on Industry Applications

$$\begin{cases}\mathbf{E}_s^*(s)\text{-}\mathbf{U}_1(s)=\left[\mathbf{I}_1(s)+\mathbf{I}_2(s)+...+\mathbf{I}_n(s)\right]\mathbf{Z}_{01}^*(s)\\ \mathbf{U}_1(s)\text{-}\mathbf{U}_2(s)=\left[\mathbf{I}_2(s)+...+\mathbf{I}_n(s)\right]\mathbf{Z}_{12}^*(s)\\ \cdots\\ \mathbf{U}_{n-1}(s)\text{-}\mathbf{U}_n(s)=\mathbf{I}_n(s)\mathbf{Z}_{n-1,n}^*(s)\end{cases} \tag{4}$$

Equation (4) is added item by item, giving

$$\begin{cases}\mathbf{E}_s^*\text{-}\mathbf{U}_1=(\mathbf{I}_1+\cdots+\mathbf{I}_n)\mathbf{Z}_{01}^*\\ \mathbf{E}_s^*\text{-}\mathbf{U}_2=(\mathbf{I}_1+\cdots+\mathbf{I}_n)\mathbf{Z}_{01}^*+(\mathbf{I}_2+\cdots+\mathbf{I}_n)\mathbf{Z}_{12}^*\\ \cdots\\ \mathbf{E}_s^*\text{-}\mathbf{U}_n=(\mathbf{I}_1+\cdots+\mathbf{I}_n)\mathbf{Z}_{01}^*+(\mathbf{I}_2+\cdots+\mathbf{I}_n)\mathbf{Z}_{12}^*+\cdots+\mathbf{I}_n\mathbf{Z}_{n-1,n}^*\end{cases} \tag{5}$$

Referring to (2), (5) can be converted into the *dq* framework and the small-signal model can be then derived. The superscript *m* is used to distinguish multi-train from single train. Then, the $2n\times 2n$ order network impedance matrix $\mathbf{Z}_s^{*m}(s)$ in the *dq* framework is

$$\begin{bmatrix}\Delta u_{1d}\\ \Delta u_{1q}\\ \cdots\\ \Delta u_{nd}\\ \Delta u_{nq}\end{bmatrix}=\begin{bmatrix}\mathbf{Z}_{(01)dd}^* & \mathbf{Z}_{(01)dq}^* & \cdots & \mathbf{Z}_{(01)dd}^* & \mathbf{Z}_{(01)dq}^*\\ \mathbf{Z}_{(01)dd}^* & \mathbf{Z}_{(01)dq}^* & \cdots & \mathbf{Z}_{(01)qd}^* & \mathbf{Z}_{(01)qq}^*\\ \cdots & \cdots & \cdots & \cdots & \cdots\\ \mathbf{Z}_{(01)dd}^* & \mathbf{Z}_{(01)dq}^* & \cdots & \sum_{i}^{i=1,\cdots,n}\mathbf{Z}_{(i-1,i)dd}^* & \sum_{i}^{i=1,\cdots,n}\mathbf{Z}_{(i-1,i)dq}^*\\ \mathbf{Z}_{(01)qd}^* & \mathbf{Z}_{(01)qq}^* & \cdots & \sum_{i}^{i=1,\cdots,n}\mathbf{Z}_{(i-1,i)qd}^* & \sum_{i}^{i=1,\cdots,n}\mathbf{Z}_{(i-1,i)qq}^*\end{bmatrix}\begin{bmatrix}\Delta i_{1d}\\ \Delta i_{1q}\\ \cdots\\ \Delta i_{nd}\\ \Delta i_{nq}\end{bmatrix} \tag{6}$$

$$\Rightarrow \Delta\mathbf{U}^m(s)=\mathbf{Z}_s^{*m}(s)\Delta\mathbf{I}^m(s)$$

where $\Delta\mathbf{U}^m(s)$ is the output voltage vector containing the input voltage $\Delta\mathbf{U}_i(s)$, $\Delta\mathbf{I}^m(s)$ is the input current vector representing the input current $\Delta\mathbf{I}_i(s)$.

Similarly, for each HST in Fig.7, the admittance matrix of the HSTs can be written as (7)

$$\begin{bmatrix}\mathbf{I}_1(s)\\ \mathbf{I}_2(s)\\ \cdots\\ \mathbf{I}_n(s)\end{bmatrix}=\begin{bmatrix}\mathbf{Y}_{11}(s) & \mathbf{Y}_{12}(s) & ... & \mathbf{Y}_{1n}(s)\\ \mathbf{Y}_{21}(s) & \mathbf{Y}_{22}(s) & ... & \mathbf{Y}_{2n}(s)\\ ... & ... & ... & ...\\ \mathbf{Y}_{n1}(s) & \mathbf{Y}_{n2}(s) & ... & \mathbf{Y}_{nn}(s)\end{bmatrix}\begin{bmatrix}\mathbf{U}_1(s)\\ \mathbf{U}_2(s)\\ ...\\ \mathbf{U}_n(s)\end{bmatrix} \tag{7}$$

The diagonal element $\mathbf{Y}_{ii}(s)$ is equal to the self-admittance of the *i*-th HST, representing the influence of the input voltage $\mathbf{U}_i(s)$ on the input current $\mathbf{I}_i(s)$. $\mathbf{Y}_{ij}(s)$ is the mutual-admittance between the *i*-th and *j*-th HSTs, that is, the influence of the other HST's input voltages $\mathbf{U}_j(s)$ on the studied input current $\mathbf{I}_i(s)$. Different from the grid-connected inverters shown in [36], the HST is regarded as a load absorbing the active power from the traction network. If the regenerative braking mode is not considered, there are no coupling between every branch current $\mathbf{I}_i(s)$, which means the mutual-admittance is $\mathbf{Y}_{ij}(s)=0$. Referring to (1), the $2n\times 2n$ order HSTs admittance matrix $\mathbf{Y}_{train}^m(s)$ in the *dq* framework is then rearranged as

$$\begin{bmatrix}\Delta i_{1d}\\ \Delta i_{1q}\\ ...\\ \Delta i_{nd}\\ \Delta i_{nq}\end{bmatrix}=\begin{bmatrix}Y_{(1,1)dd} & Y_{(1,1)dq} & \cdots & 0 & 0\\ Y_{(1,1)qd} & Y_{(1,1)qq} & \cdots & 0 & 0\\ \cdots & \cdots & \cdots & \cdots & \cdots\\ 0 & 0 & \cdots & Y_{(n,n)dd} & Y_{(n,n)dq}\\ 0 & 0 & \cdots & Y_{(n,n)qd} & Y_{(n,n)qq}\end{bmatrix}\begin{bmatrix}\Delta u_{1d}\\ \Delta u_{1q}\\ ...\\ \Delta u_{nd}\\ \Delta u_{nq}\end{bmatrix} \tag{8}$$

$$\Rightarrow \Delta\mathbf{I}^m(s)=\mathbf{Y}_{train}^m(s)\Delta\mathbf{U}^m(s)$$

B. Impedance-Based Stability Assessment Method

The impedance or admittance matrix of the traction network and multi-train in the *dq*-domain are both $2n\times 2n$ matrices, as expressed in (6) and (8). The output voltage and current used in the network impedance matrix and multi-train admittance matrix are the same, their small signal variations can depict a multivariable feedback system, as shown in Fig. 8(a), where the input of closed loop system is the network voltage $\Delta\mathbf{E}_s^*(s)$, the output is the network current $\Delta\mathbf{I}^m(s)$. It can be seen as a block diagram generated by the Thevenin representation of Fig. 8(b).

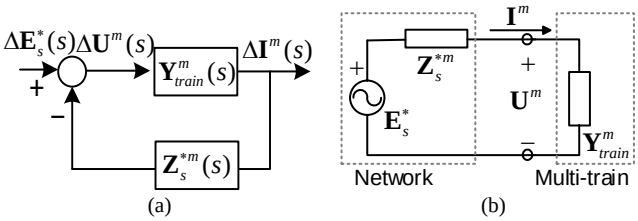

Fig. 8. Multi-train modeling (a) block diagram of multivariable feedback system; (b) Thevenin representation of the MTNS.

Then, the closed loop transfer matrix of the MTNS can be expressed as

$$\mathbf{H}(s)=\frac{\mathbf{Y}_{train}^m(s)}{\mathbf{I}_{2n}+\mathbf{Y}_{train}^m(s)\cdot\mathbf{Z}_s^{*m}(s)} \tag{9}$$

where $\mathbf{I}_{2n}$ is a $2n\times 2n$ unity diagonal matrix. As the number of HSTs increase, the characteristic locus of the minor-loop gain $\mathbf{Y}_{train}^m(s)\mathbf{Z}_s^{*m}(s)$ will increase. Correspondingly, Pole-zero analysis is a powerful tool to investigate the linear system stability. To keep a multivariable feedback system stable, all the poles of the closed loop transfer matrix must lie in the left-half of the complex s-plane [37]. Therefore, the MTNS is stable if and only if the closed loop transfer matrix in (9) have no poles located in the right half plane (RHP). Notice that the network feedback transfer matrix $\mathbf{Z}_s^{*m}(s)$ has no poles and is naturally stable. Additionally, the transfer matrix of multi-train $\mathbf{Y}_{train}^m(s)$ will be stable in a suitable parameter range. Therefore, the possible RHP poles of the closed loop transfer matrix $\mathbf{H}(s)$ are the main reasons for the instability phenomenon.

V. Influence Factors of the Harmonic Instability

To investigate the harmonic instability of the MTNS, the trajectory of poles of the closed loop transfer matrix $\mathbf{H}(s)$ in (9) are computed to evaluate the harmonic stability. The network and controller parameters of the simulation and experimental system are listed in Appendix B.

A. *Impact of the Number of HSTs*

There are usually no more than three running HSTs in a same power supply phase during the normal operation modes. Fig. 9 depicts the poles traces of the MTNS as the HST number increases, where the HSTs are coupled due to the network impedance. There are some conjugate pairs dominating the high frequency (higher than several hundred rad/s) stability characteristic, and the other conjugate pairs are dominating the low frequency (below 50 rad/s) stability characteristic. In Fig. 9, an increasing number of HSTs pose more complex closed loop transfer matrix and more poles. The poles traces of an individual HST and two HSTs are located in the left-half plane and indicate that the individual HST and two HSTs are able to operate stably. Once the number of HSTs exceed three, some poles are located in the right-half plane, which means the system will be unstable.

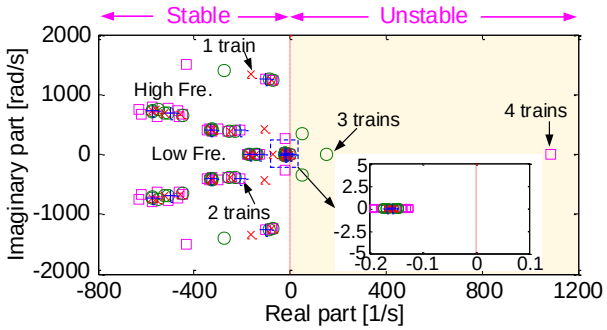

Fig. 9. Trajectory of poles as the HST numbers are increased from 1 to 4. The red spot '×' denotes a single HST, the blue spot '+', green spot '○' and purple spot '□' denote the two HSTs, three HSTs and four HSTs, respectively.

Note that the valid frequency width of the multi-train admittance matrix is up to the Nyquist frequency $f_s/2$ as the PWM modulation uses the average model. In addition, for a single-phase ac system, the *dq* decoupling method is commonly used to obtain the steady-state operating points. The trajectory of poles in Fig. 9 are all located in an available frequency range, illustrating that the impedance-based is efficient.

B. *Impact of Controller Parameters*

The trajectory of the poles when changing proportional gain of the CC, PLL and VC are shown in Fig. 10. Two running HSTs are considered and the initial parameters listed in Appendix B are used. In Fig. 10(a), the proportional gain of the current controller (Kp_{CC}) ranges from 3 to 7 by a step of 1, where a high frequency complex conjugate pole moves toward the RHP as Kp_{CC} increases. The system will be unstable once the Kp_{CC} is more than 4.05. Similarly, in Fig. 10(b) and (c), the proportional gain of the PLL (Kp_{PLL}) and VC (Kp_{VC}) ranges from 0.5 to 4.5 by a step of 1, and 0.4 to 2 by a step of 0.4, respectively. The high frequency complex conjugate poles move toward the RHP as Kp_{PLL} decreases or Kp_{VC} increases. When Kp_{PLL} is smaller than 0.75 or Kp_{VC} is larger than 1.25, the system will have some high frequency poles located in the RHP, indicating the occurrence of the harmonic instability. In addition, it can be seen that the low frequency poles are insensitive to the controller parameter. Thus, the high frequency complex conjugate poles dominate the harmonic instability phenomenon in the condition.

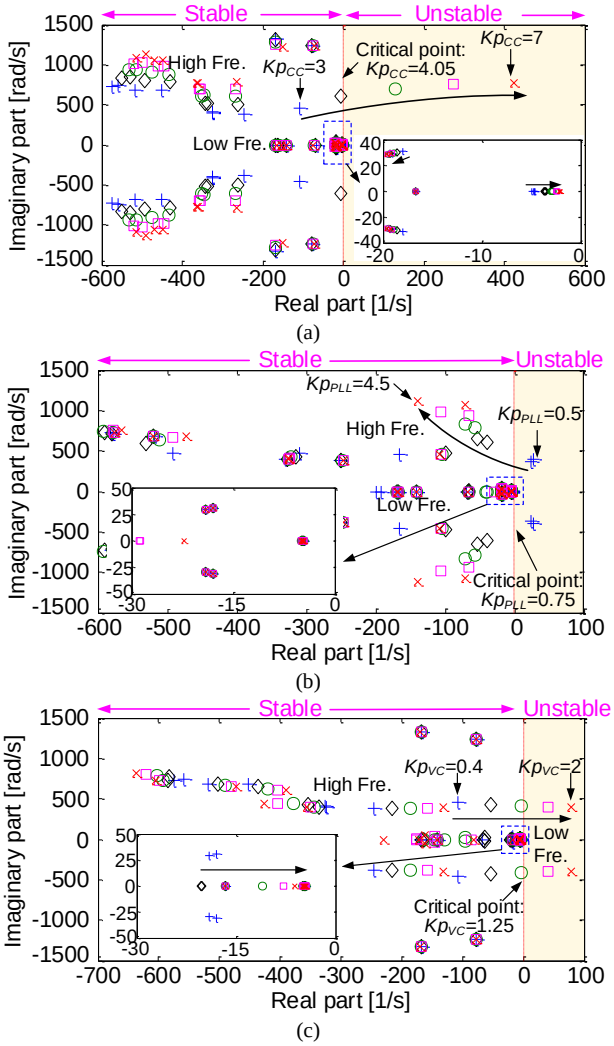

Fig. 10. Trajectory of poles when increasing (a) Kp_{CC} ($3 < Kp_{CC} < 7$, step: 1), (b) Kp_{PLL} ($0.5 < Kp_{PLL} < 4.5$, step: 1) and (c) Kp_{VC} ($0.4 < Kp_{VC} < 2$, step: 0.4). The blue spot '+' denotes the initial value, then the black spot '◇', the green spot '○', purple spot '□' and red spot '×' denote the second, third, fourth and fifth calculation, respectively.

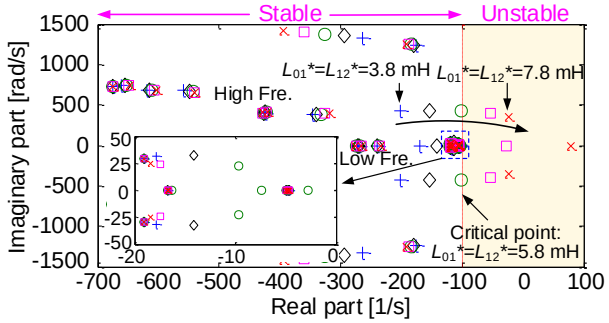

Fig. 11. Trajectory of poles when increasing the network inductances L_{01}^*, L_{12}^* ($3.8\ \mathrm{mH} < L_{01}^*, L_{12}^* < 7.8\ \mathrm{mH}$, step with 1 mH).

C. Impact of the Network Inductance

The network impedance consists of the resistive and inductive components. To explain the effects of the network inductance (L_{01}^*, L_{12}^*) on harmonic instability, the trajectory of poles with different network inductance is given in Fig. 11. When L_{01}^* and L_{12}^* are synchronization increased from 3.8 mH to 7.8 mH, a high frequency complex conjugate pole and a real root move toward the RHP as L_{01}^*, L_{12}^* increases meanwhile the threshold of the instability is 5.8 mH.

VI. Simulations and Experiments

A. Simulation Results

In order to validate the proposed theoretical analysis, time-domain simulations of the MTNS are shown in Fig. 7 and the control system in Fig. 3 is performed based on Matlab/ Simulink software. The parameters given in TABLE BI of Appendix B are fully considered.

Fig. 12 illustrates the simulation results when a single HST system is in the unstable condition. Fig. 12(a) denotes that Kp_{CC} increases from 3 to 15 at 0.25s and Fig. 12(b) depicts that L_{01}^* increases from 3.8 mH to 20 mH at 0.1s. The harmonic components of the voltage are amplified and the system becomes unstable, which agrees with the GNC analysis in Fig. 6.

The simulation results of increasing the number of the connected HSTs are shown in Fig. 13. The HST #1 and HST #2 are connected stably. Once the HST #3 is activated and connected into catenary at 0.2 s, the harmonic components of the network voltage are observed. When the HST #4 is activated and connected in the catenary, the harmonic components are amplified and the whole system becomes unstable. The result agrees well with the poles in Fig. 9.

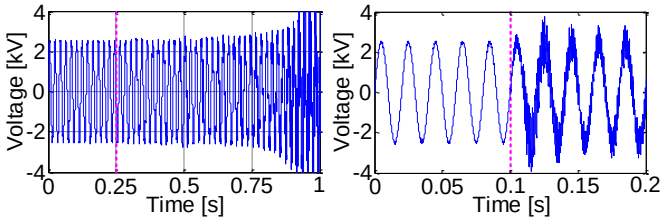

Fig. 12. Unstable case of a single HST network system: (a) Kp_{CC} increases from 3 to 15 at 0.25s; (b) L_{01}^* increasing from 3.8 mH to 20 mH at 0.1s.

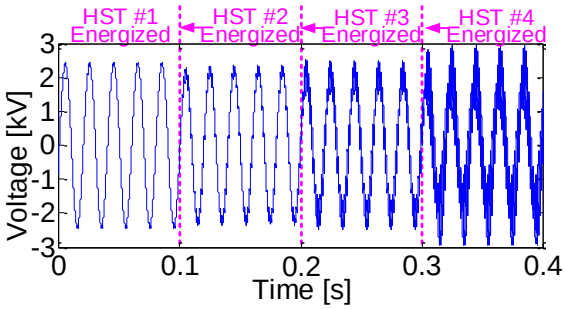

Fig. 13. Simulation results as the number of HSTs are increased.

Fig. 14(a), (b) and (c) depict the simulation results when the proportional gain Kp_{CC} , Kp_{PLL} and Kp_{VC} in the CC, PLL and VC are in the unstable region. The interaction system will turn to become unstable after changing the corresponding parameters of these controllers. In Fig. 14(a), (b) and (c), the harmonic components of the network voltage are gradually amplified and the system becomes unstable. The results demonstrate the theoretical result in Fig. 10. Meanwhile, the harmonic instability in the MTNS is mainly caused by the instability behavior of the controller.

As shown in Fig. 14(d), the harmonic components of the network voltage are amplified after synchronization increases the network inductance L_{01}^* and L_{12}^* from 3.8 mH to 6.8 mH at 0.1s. The results agree well with the theoretical results shown in Fig. 11.

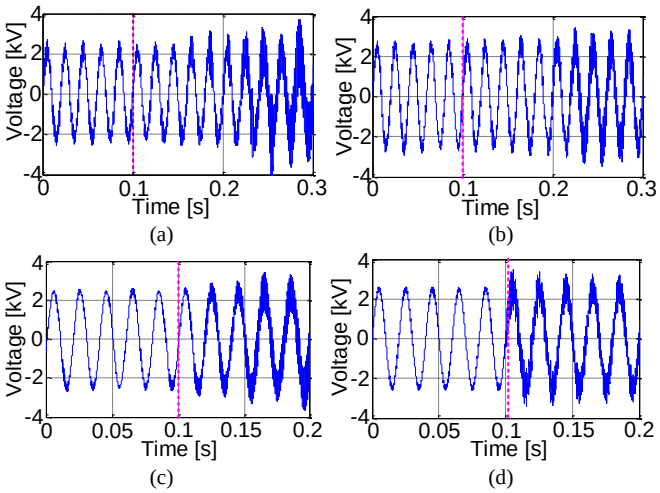

Fig. 14. Simulation results when a step change of Kp_{CC} , Kp_{PLL} , Kp_{VC} and network impedance: (a) Kp_{CC} increases from 3 to 5 at 0.1s; (b) Kp_{PLL} decreases from 6 to 0.5 at 0.1s; (c) Kp_{VC} increases from 0.4 to 1.4 at 0.1s; (d) The L_{01}^* and L_{12}^* synchronization increase from 3.8 mH to 6.8 mH at 0.1s.

B. Experimental Results

To further validate the proposed impedance calculation method, a scaled down experimental platform with two HSTs are carried out. The hardware picture and circuit configuration of the experimental platform is shown in Fig. 15 and its parameters are listed in TABLE BI. In this experimental system, the rated power of each HST is 88.2 W with 21 V ac input voltage and 42 V dc output voltage. Meanwhile, its input voltage is isolated through a single-phase step-down transformer (240 V/21 V). Additionally, the IGBTs (1MBH60D-100) are chosen for the 4QC and the TX-DA962D4 is used as drive circuit. The switching frequency is set to 1250 Hz. SC is the signal conditioner. The control system is implemented into the DSP (TMS320F28335). The waveforms are recorded by the oscilloscope (Agilent DSO-X3034A). The control parameters of the system can be altered in the host computer through bluetooth module.

This article has been accepted for publication in a future issue of this journal, but has not been fully edited. Content may change prior to final publication. Citation information: DOI 10.1109/TIA.2018.2793843, IEEE Transactions on Industry Applications

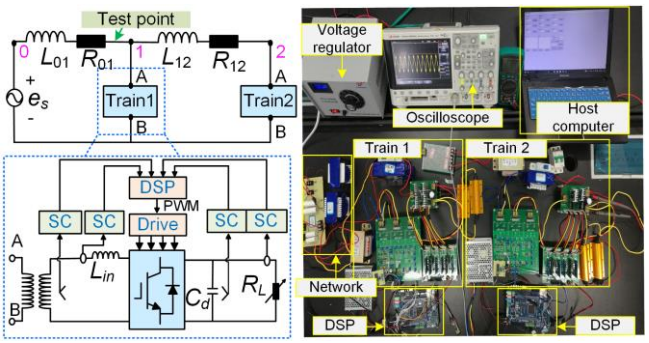

Fig. 15. Experimental setup of the MTNS.

Based on the impedance-based stability assessment method in Section IV, the trajectory of the poles with two HSTs when increasing the values of the Kp_{CC} and network inductances are shown in Fig. 16. As a result, with the increase of Kp_{CC} from 6.5 to 10.5 by a step of 1, a complex conjugate pole moves toward the right half-plane (unstable region). Similarly, with the synchronization increase of L_{01}^{*} and L_{12}^{*} from 3.2 mH to 7.2 mH by a step of 1 mH, a complex conjugate pole and a real root move toward the right half-plane. When Kp_{CC} is larger than 7.75 or L_{01}^{*} and L_{12}^{*} are larger than 5 mH, the system will have a high frequency complex conjugate pole located in the RHP, indicating the occurrence of the harmonic instability.

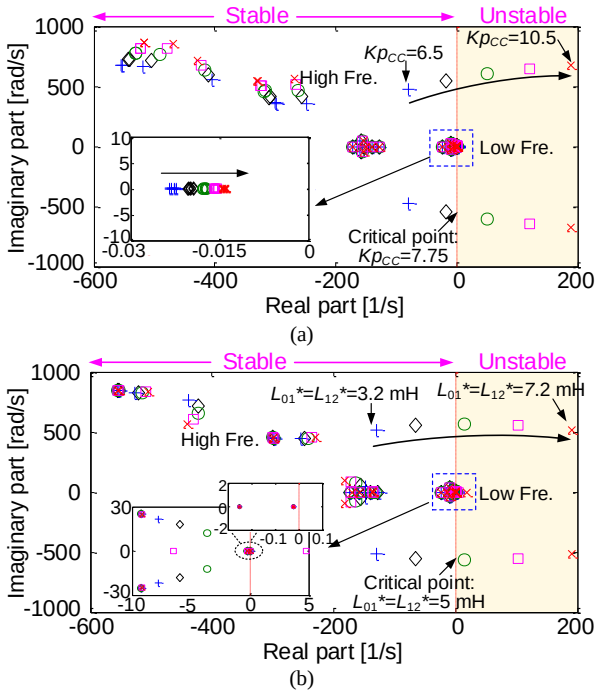

Fig. 16. Trajectory of poles for an increase of (a) the current controller proportional gain Kp_{CC} and (b) the network inductances L_{01}^{*}, L_{12}^{*}.

The experimental results when changing Kp_{CC} of paralleled two HSTs are shown in Fig. 17. Two sets of Kp_{CC}, i.e., $Kp_{CC}=6.5$ and $Kp_{CC}=9$, are tested. It is clear that the voltage and current contain a large number of harmonic components and the experimental system becomes unstable when Kp_{CC} is increased to 9, which is closely correlated with the theoretical analysis in Fig. 16(a).

Fig. 18 depicts the experimental results of different network inductances with two paralleled HSTs. Three sets of L_{01}^{*}, L_{12}^{*}, i.e., $L_{01}^{*}=L_{12}^{*}=7.2\ mH/3.2\ mH/7.2\ mH$, are tested. The harmonic components of the voltage and current will be gradually amplified when L_{01}^{*}, L_{12}^{*} are increased to 7.2 mH. Therefore, a reduced network inductance is needed to inhibit harmonic stability. It agrees with the theoretical results shown in Fig. 16(b).

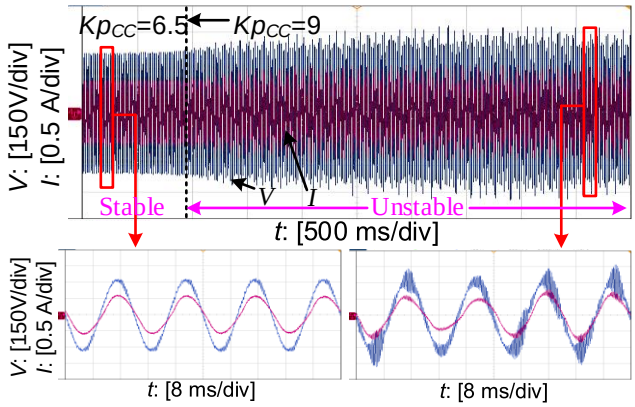

Fig. 17. Measured network voltage and current when a step change of Kp_{CC} from 6.5 to 9.

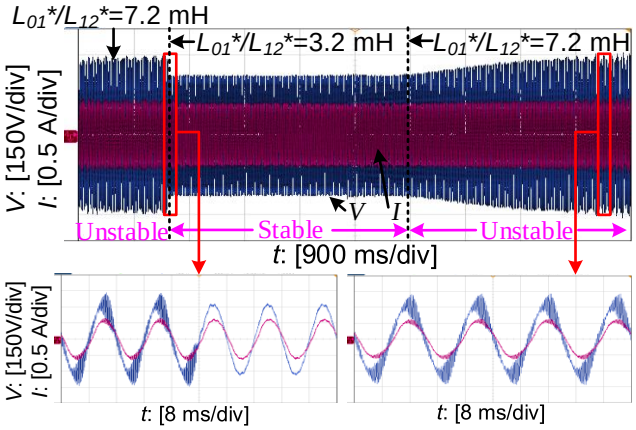

Fig. 18. Measured network voltage and current with a step change of network inductances L_{01}^{*}, L_{12}^{*}.

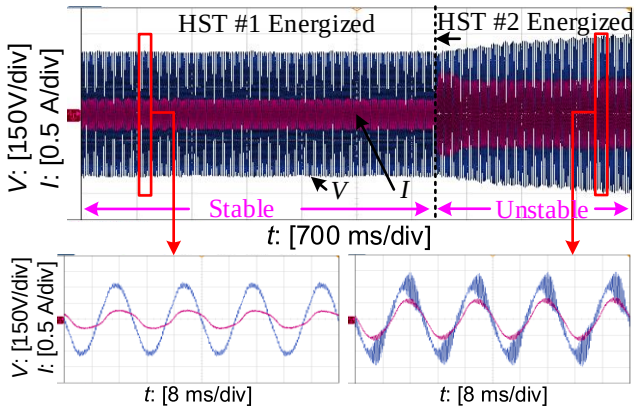

Fig. 19. Measured network voltage and current as the number of HSTs are increased.

Fig. 19 depicts the experimental results with different numbers of HSTs. The Kp_{CC} of two HSTs are both set to 9 for obtaining an unstable condition. It can be seen that a single HST is stable. Once the HST #2 is activated and connected to the network, the harmonic is amplified and the whole system becomes unstable. The results indicate the number of HSTs have a significant effect on stability.

C. Summary

The harmonic instability is closed related to harmonic resonance phenomenon that the resonance is easily arisen when the interaction system is unstable. In fact, different influential factors are equivalent to regulate the impedance transfer matrix of the interaction system, which can further change the poles distribution of the closed loop transfer matrix. Therefore, it may generate an unstable region by continuously changing the network parameters and controller parameters of the HSTs. The harmonic instability region with different system parameters are not the same, but the simulations and experiments have the same trend with the calculations, which verify the analysis and the proposed method. The unstable regions in the calculations, simulations and experiments are listed in TABLE I. For a specific railway line analysis, the system stability can be evaluated with specific parameters by using the proposed impedance-based model.

TABLE I
HARMONIC INSTABILITY FACTORS

Subject	Factor	Instability region
Simulation	Number of the HSTs	> 2
	CC parameter Kp_{CC}	≥ 4.05
	PLL parameter Kp_{PLL}	≤ 0.75
	VC parameter Kp_{VC}	≥ 1.25
	Network inductance L_{01}^{*}, L_{12}^{*}	≥ 5.8 mH
Experiment	Number of the HSTs	> 2
	CC parameter Kp_{CC}	≥ 7.75
	Network inductance L_{01}^{*}, L_{12}^{*}	≥ 5 mH

VII. DISCUSSION AND SUGGESTIONS

A. Differences Between Harmonic Instability and Harmonic Resonance

The harmonic resonance risk is inherent in any industrial power systems. However, not all resonances can cause serious harmonic instability problem. The resonance may easily generate the harmonic instability problem with active power-electronics devices because of the possible unstable interactions between the traction network and the HST. The standard EN50388-2 provides a method to suppress the harmonic instability problems in the train and network interaction system [5]: An electrified traction vehicle shall be passive above a certain frequency f_L, and the lowest resonance in the traction network shall be greater than f_L. This is a conservative method.

The harmonic voltage spectrum in the stable and unstable condition are plotted in Fig. 20 demonstrates that not all resonance will excite the harmonic instability only if the high frequency poles are located in the RHP. When the interaction system has no high frequency poles in the RHP, as shown in Fig. 20(a), the interaction system is stable and there are harmonic resonances around the 29 pu, 49 pu and 51pu. If the interaction system has high frequency poles in the RHP, the harmonic voltage around 29 pu will be gradually amplified, as shown in Fig. 20(b), but the harmonic voltage magnitude around 49 pu and 51 pu are still there.

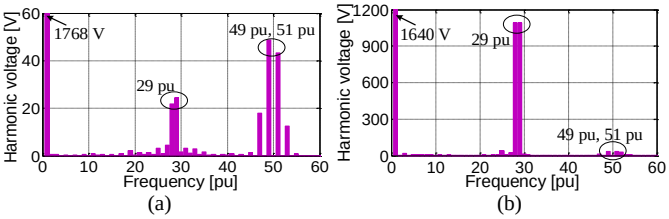

Fig. 20. Harmonics voltage spectrum with different pole distributions: (a) no high frequency poles located in the RHP (stable); (b) high frequency poles located in the RHP (unstable).

B. Mitigation Suggestions for the Harmonic Instability

The impedance-based model of the interaction system plays a dominant role when studying the harmonic instability. Based on the obtained results and in order to avoid and attenuate the harmonic instability problems, the following methods can be adopted:

1) *Influential parameters adjustment*. The harmonic instability in the interaction system of different HST and network parameters, which has an unstable region as shown in TABLE I. If the parameters fall into an unstable region, the system will be unstable, then the harmonic voltage or current will be gradually amplified. In addition, reducing or increasing those parameters can help them escape from the unstable region. Fig. 21 depicts the experimental result of decreasing the proportional gain of the CC. The harmonic instability phenomenon got a good inhibition, which verified the theoretical result in Fig. 16(a). Therefore, it is necessary to select a suitable bandwidth of the control loops.

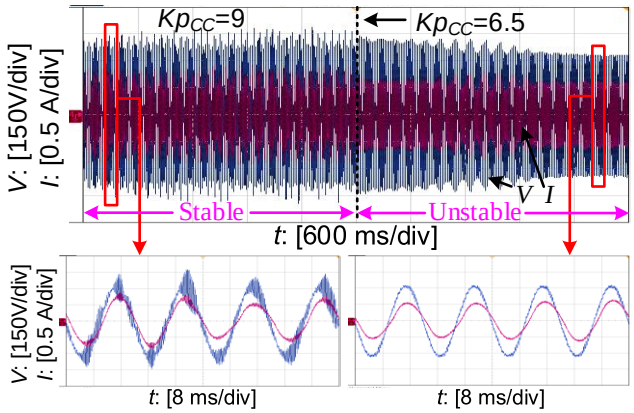

Fig. 21. Measured network voltage and current with a step change of current controller proportional gain Kp_{CC} from 9 to 6.5.

2) *Additional mitigation devices installation*. By using a damping resistor in series with the filter capacitor C and LCL filter to damp the unstable poles and decrease the resonance

This article has been accepted for publication in a future issue of this journal, but has not been fully edited. Content may change prior to final publication. Citation information: DOI 10.1109/TIA.2018.2793843, IEEE Transactions on Industry Applications

peak in the Bode diagram is a possibility [38]. Fig. 22 depicts the experimental results of putting in first-order high-pass filter, which has a better performance in mitigating harmonic instability. However, the additional impedance will generate the power losses and decrease the efficiency of the power system. Hence, the method of additional passive damping is applicable for small or middle photovoltaic and wind power system.

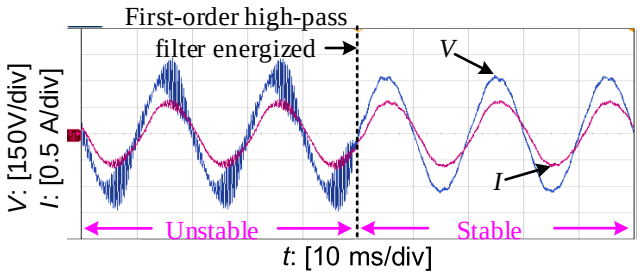

Fig. 22. Measured network voltage and current when a first-order high-pass filter is energized.

3) *Traction network enhancement*. the HST and network interaction system is prone to the instability problem under a weak network condition [14]. The experimental results in Fig. 18 verify this conclusion. Therefore, the economy, reliability and stability should be comprehensively considered. During the line design stage or transformation stage, the traction network impedance (especially for the network inductance) can be reduced for a more stable system.

VIII. Conclusions

In this paper, in order to investigate the formation and influential factors of the harmonic instability phenomena in the electrified railways, an impedance-based method and the interaction between multi-train and traction network is presented. Firstly, the impedance model of the HST includes a phase-locked loop, current controller, and voltage controller. Then, an overall impedance model containing the multi-train and traction network is proposed. The harmonic instability is well assessed by analyzing the trajectory of poles in the closed loop impedance transfer matrix. The analytical results present the controller's parameters of HST, the number of HSTs and the traction network inductance all have an essential effect on the harmonic instability in the MTNS. The proposed method of harmonic instability and available influential factors have been validated through simulations and experiments. If possible, mitigation measures, including influential parameters adjustment, additional mitigation devices installation and traction network enhancement can be options to solve the problem.

Appendix A
DQ-Domain Admittance Modeling of the HST

A. Phase-Locked Loop Model

The voltage synchronization control block diagram is shown in Fig. A1. Steinar Danielsen in [8] introduced the SOGI transfer function in (10).

$$\mathbf{H}_{eSOGI}=\begin{bmatrix} H_{eSOGI} & 0 \\ 0 & H_{eSOGI} \end{bmatrix}, H_{eSOGI}=\frac{1}{\frac{s}{K_{eSOGI}}\left(\frac{1}{w_0}+\frac{T_0}{8}\right)+1} \tag{10}$$

where K_{eSOGI} represents the proportional gain of the SOGI in the voltage synchronization system, w_0 is the fundamental angular frequency and T_0 is the fundamental sampling time.

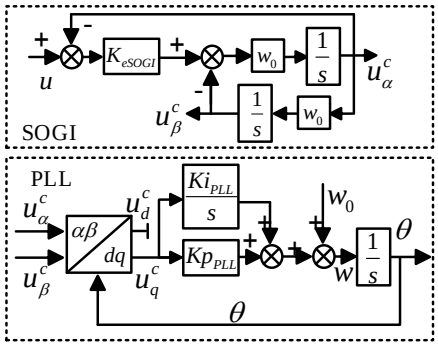

Fig. A1. Control block diagram of voltage synchronization system.

From Fig. A1, introducing the phase-locked error $\Delta\theta=\theta-\theta_0$ and $w_0=s\theta_0$, one can obtain

$$s\theta=w_0+\underbrace{\left(Kp_{PLL}+\frac{Ki_{PLL}}{s}\right)}_{F_{PLL}}u_q^c \Rightarrow s\Delta\theta=F_{PLL}u_q^c \tag{11}$$

where the error angle $\Delta\theta$ is sufficiently small and there exists the following relationship

$$\begin{aligned}&\mathbf{U}^c=\mathbf{H}_{eSOGI}e^{-j\Delta\theta}\mathbf{U}\approx\mathbf{H}_{eSOGI}(1-j\Delta\theta)(\Delta\mathbf{U}+\mathbf{U}_0)\\&\Rightarrow\mathbf{U}^c\approx\mathbf{H}_{eSOGI}(\Delta\mathbf{U}-j\mathbf{U}_0\Delta\theta)\end{aligned} \tag{12}$$

The u_{q0} is equal to zero in steady-state, so $\mathbf{U}_0=u_{d0}$ and $u_q^c\approx H_{eSOGI}(\Delta u_q-u_{d0}\Delta\theta)$ can be obtained. Then together with (11), $\Delta\theta$ can be written as

$$\Delta\theta=\underbrace{\frac{F_{PLL}H_{eSOGI}}{s+u_{d0}F_{PLL}H_{eSOGI}}}_{G_{PLL}}\Delta u_q \tag{13}$$

Inserting (13) into (12), the voltage transfer matrix of the PLL is

$$\begin{bmatrix}\Delta u_d^c\\ \Delta u_q^c\end{bmatrix}=\underbrace{\begin{bmatrix}H_{eSOGI} & 0\\ 0 & H_{eSOGI}-H_{eSOGI}u_{d0}G_{PLL}\end{bmatrix}}_{G_{uPLL}(s)}\begin{bmatrix}\Delta u_d\\ \Delta u_q\end{bmatrix} \tag{14}$$

Correspondingly, the current synchronization system has the same structure with the voltage synchronization system apart from the PLL. Referring to (12) and ignoring the effect of the SOGI on network current, the current of the different frames can be linearized as

$$\mathbf{I}^c=\mathbf{H}_{iSOGI}e^{-j\Delta\theta}\mathbf{I}\Rightarrow\mathbf{I}^c\approx\Delta\mathbf{I}\text{-}\mathbf{H}_{iSOGI}j\mathbf{I}_0\Delta\theta \tag{15}$$

Inserting (13) to (15), the transfer function of current synchronization system can be written in small-signal form as

$$\begin{bmatrix}\Delta i_d^c\\ \Delta i_q^c\end{bmatrix}=\begin{bmatrix}\Delta i_d\\ \Delta i_q\end{bmatrix}-\underbrace{\begin{bmatrix}0 & -i_{q0}H_{iSOGI}G_{PLL}\\ 0 & i_{d0}H_{iSOGI}G_{PLL}\end{bmatrix}}_{G_{iPLL}(s)}\begin{bmatrix}\Delta u_d\\ \Delta u_q\end{bmatrix} \tag{16}$$

where $i_{d0}=P_0/u_{d0}$ and $i_{q0}=Q_0/u_{d0}$ are steady-state active and reactive currents in the network side. H_{iSOGI} is the proportional gain of SOGI in the current synchronization system.

B. Current Controller Model

Fig. A2 depicts the current controller. Applying the Kirchhoff law in Fig. 3, the dynamic equations in small-signal form of the 4QC *dq* frame can be given by

$$\begin{bmatrix}\Delta v_d^c\\ \Delta v_q^c\end{bmatrix}=\begin{bmatrix}\Delta u_d^c\\ \Delta u_q^c\end{bmatrix}-\begin{bmatrix}R_{in}+sL_{in} & -w_0L_{in}\\ w_0L_{in} & R_{in}+sL_{in}\end{bmatrix}\begin{bmatrix}\Delta i_d^c\\ \Delta i_q^c\end{bmatrix} \tag{17}$$

The decoupling is added to the control loop in the form of an inner positive-feedback loop with a gain jw_0L_{in}. From Fig. A2, the voltage reference $\mathbf{U}^{ref}$ can be derived as

$$\begin{aligned}\begin{bmatrix}\Delta u_d^{ref}\\ \Delta u_q^{ref}\end{bmatrix}=&\begin{bmatrix}\Delta u_d^c\\ \Delta u_q^c\end{bmatrix}-\underbrace{\begin{bmatrix}Kp_{CC}+\dfrac{Ki_{CC}}{s} & 0\\ 0 & F_{CC}\end{bmatrix}}_{F_{CC}}\begin{bmatrix}\Delta i_d^{ref}-\Delta i_d^c\\ \Delta i_q^{ref}-\Delta i_q^c\end{bmatrix}\\ &-\begin{bmatrix}0 & -w_0L_{in}\\ w_0L_{in} & 0\end{bmatrix}\begin{bmatrix}\Delta i_d^c\\ \Delta i_q^c\end{bmatrix}\end{aligned} \tag{18}$$

The input voltage *v* of the 4QC is generated by PWM modulation, considering the impact of the delay time T_d [25], we have

$$\begin{bmatrix}\Delta v_d^c\\ \Delta v_q^c\end{bmatrix}=\begin{bmatrix}G_d & 0\\ 0 & G_d\end{bmatrix}\begin{bmatrix}\Delta u_d^{ref}\\ \Delta u_q^{ref}\end{bmatrix},\quad G_d=\frac{1}{T_ds+1} \tag{19}$$

where the time delay function G_d is a first-order function due to the single-updated PWM and we have T_d=1.5/f_s, f_s is the switching frequency of the 4QC.

Equations (17)~(19) can be combined into (20).

$$\begin{cases}\begin{bmatrix}\Delta i_d^c\\ \Delta i_q^c\end{bmatrix}=\underbrace{\mathbf{H}_{CC}^{-1}\begin{bmatrix}1-G_d & 0\\ 0 & 1-G_d\end{bmatrix}}_{\mathbf{Y}_{CC}}\begin{bmatrix}\Delta u_d^c\\ \Delta u_q^c\end{bmatrix}+\underbrace{\mathbf{H}_{CC}^{-1}\begin{bmatrix}G_dF_{CC} & 0\\ 0 & G_dF_{CC}\end{bmatrix}}_{\mathbf{G}_{CC}}\begin{bmatrix}\Delta i_d^{ref}\\ \Delta i_q^{ref}\end{bmatrix}\\ \mathbf{H}_{CC}(s)=\begin{bmatrix}G_dF_{CC}+R_{in}+sL_{in} & (G_d-1)w_0L_{in}\\ (1-G_d)w_0L_{in} & G_dF_{CC}+R_{in}+sL_{in}\end{bmatrix}\end{cases} \tag{20}$$

where $\mathbf{Y}_{CC}(s)$ and $\mathbf{G}_{CC}(s)$ are the inner (seen from the voltage *u*) closed loop input admittance and transfer function.

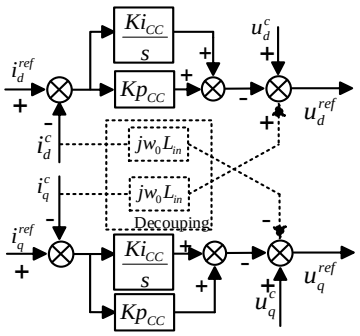

Fig. A2. Structure of the current controller (CC).

C. Voltage Controller Model

Fig. A3 depicts the structure of voltage controller. The output of the VC is the active current reference i_d^{ref} for the CC and i_q^{ref} is set to zero for the unity power factor. In order to eliminate the dependence on the dc-link steady-state operating point v_{dc0}, it is an effective method to use the 'energy' error $\left[(v_{dc}^{ref})^2-v_{dc}^2\right]/2$ instead of dc voltage error $v_{dc}^{ref}-v_{dc}$ [21].

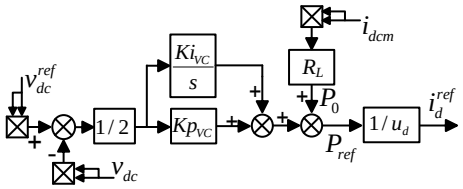

Fig. A3. Structure of the voltage controller (VC).

The dc-link voltage reference v_{dc}^{ref} is equal to steady-state voltage v_{dc0} in steady state. From Fig. A3, the active power reference and its linearized expression can be calculated as

$$\begin{aligned}P_{ref}=&\underbrace{\left(Kp_{VC}+\frac{Ki_{VC}}{s}\right)}_{F_{VC}}\frac{(v_{dc}^{ref})^2-(v_{dc})^2}{2}+P_0\\ \Rightarrow\Delta P_{ref}=&-F_{VC}v_{dc0}\Delta v_{dc}\end{aligned} \tag{21}$$

where the load power $P_0=v_{dc}i_{dcm}=i_{dcm}^2R_L=v_{dc}^2/R_L$, R_L is load resistance. The active current reference i_d^{ref} and its linearized expression Δi_d^{ref} can be given by

$$i_d^{ref}=\frac{P_{ref}}{u_d}\Rightarrow\Delta i_d^{ref}=-\frac{F_{VC}v_{dc0}}{u_{d0}}\Delta v_{dc}-\frac{P_0}{u_{d0}^2}\Delta u_d \tag{22}$$

Combining (20), the network current can be written in small-signal form as

$$\begin{aligned}\Delta i_d=&\left[\mathbf{Y}_{CC(1,1)}-\frac{P_0}{u_{d0}^2}G_{CC(1,1)}\right]\Delta u_d+\mathbf{Y}_{CC(1,2)}\Delta u_q\\ &-\frac{v_{dc0}\mathbf{G}_{CC(1,1)}F_{VC}}{u_{d0}}\Delta v_{dc}\end{aligned} \tag{23}$$

An ideal lossless model of the 4QC is assumed for simplification of modeling. Therefore, active power balance constraint between ac and dc side can be given by

$$u_di_d=\frac{1}{2}C_d\frac{dv_{dc}^2}{dt}+P_0 \tag{24}$$

where the energy stored in the dc capacitor is $C_dv_{dc}^2/2$ [21]. Equation (24) can be expressed in small-signal form as

$$\Delta P=i_{d0}\Delta u_d+u_{d0}\Delta i_d=sC_dv_{dc0}\Delta v_{dc} \tag{25}$$

Combing (23) and (25), the dc-link voltage can be written in small-signal form as

$$\Delta v_{dc}=\frac{\left[i_{d0}+u_{d0}\mathbf{Y}_{CC(1,1)}-\dfrac{P_0}{u_{d0}}\mathbf{G}_{CC(1,1)}\right]\Delta u_d+\left[u_{d0}\mathbf{Y}_{CC(1,2)}+i_{q0}\right]\Delta u_q}{v_{dc0}\left[sC_d+\mathbf{G}_{CC(1,1)}F_{VC}\right]} \tag{26}$$

Thus, insert (26) back into (22), and solve the reference

current matrix, it can be written in a small-signal form as

$$\begin{bmatrix}\Delta i_d^{ref}\\ \Delta i_q^{ref}\end{bmatrix}=\underbrace{\begin{bmatrix}-G_{VC}^d & G_{VC}^q\\ 0 & 0\end{bmatrix}}_{\mathbf{G}_{VC}(s)}\begin{bmatrix}\Delta u_d\\ \Delta u_q\end{bmatrix} \tag{27}$$

where

$$\begin{cases}G_{VC}^d=\dfrac{F_{VC}\left[i_{d0}+u_{d0}\mathbf{Y}_{CC(1,1)}\text{-}i_{d0}\mathbf{G}_{CC(1,1)}\right]}{u_{d0}\left[sC_d+\mathbf{G}_{CC(1,1)}F_{VC}\right]}+\dfrac{P_0}{u_{d0}^2}\\ G_{VC}^q=\dfrac{F_{VC}\left[i_{q0}+u_{d0}\mathbf{Y}_{CC(1,2)}\right]}{u_{d0}\left[sC_d+\mathbf{G}_{CC(1,1)}F_{VC}\right]}\end{cases} \tag{28}$$

APPENDIX B

TABLE BI
PARAMETERS FOR SIMULATION AND EXPERIMENTAL SYSTEM OF THE MTNS

Symbol	Description	Simulation Value	Experimental Value
e_S	Network voltage	25 kV	240 V
u_{d0}	*d* channel steady state voltage	1770 V	21 V
u_{q0}	*q* channel steady state voltage	0 V	0 V
k	Ratio	15.54	11.43
f_0	Grid fundamental frequency	50 Hz	50 Hz
L_{01}^* , L_{12}^* , L_{23}^*	Network inductance in the secondary side	3.8 mH, 3.8 mH, 3.8 mH	4.2 mH, 4.2 mH, 0 mH
R_{01}^* , R_{12}^* , R_{23}^*	Network resistance in the secondary side	0.2 Ω, 0.2 Ω, 0.2 Ω	0.2 Ω, 0.2 Ω, 0 Ω
L_{in}	Leakage inductance of the transformer	6 mH	14 mH
R_{in}	Leakage resistance of the transformer	0.2 Ω	0.1 Ω
C_d	DC-link capacitance	10 mF	4.4 mF
R_L	Load resistance	20 Ω	20 Ω
v_{dc0}	DC-link voltage	3600 V	42 V
P_0	Active power	648 kW	88.2 W
Q_0	Reactive power	0 kW	0 kW
f_S	Switching frequency	1250 Hz	1250 Hz
K_{eSOGI}	SOGI-voltage gain	0.8	0.8
K_{iSOGI}	SOGI-current gain	1	1
Kp_{VC}	VC-Proportional gain	0.4	0.1
Ki_{VC}	VC-Integral gain	12	0.025
Kp_{PLL}	PLL-Proportional gain	6	1
Ki_{PLL}	PLL-Integral gain	100	30
Kp_{CC}	CC-Proportional gain	3	6.5
Ki_{CC}	CC-Integral gain	0.5	0.15

Reference

[1] E. Mollerstedt and B. Bernhardsson, "Out of control because of harmonics-an analysis of the harmonic response of an inverter locomotive," *IEEE Control Syst.*, vol. 20, no. 4, pp. 70-81, Aug. 2000.

[2] J. D. Ainsworth, "Harmonic instability between controlled static convertors and a.c. networks," *Proc. Inst. of Elect. Eng.*, vol. 114, no. 7, pp. 949-957, 1967.

[3] L. H. Kocewiak, J. Hjerrild and C. L. Bak, "Wind turbine converter control interaction with complex wind farm systems," *IET Renewable Power Gener.*, vol. 7, no. 4, pp. 380-389, Jun. 2013.

[4] J. H. R. Enslin and P. J. M. Heskes, "Harmonic interaction between a large number of distributed power inverters and the distribution network," *IEEE Trans. Power Electron.*, vol. 4, no. 6, pp. 1586-1593, Nov. 2004.

[5] *EN 50388 Standard - Power Supply and Rolling Stock - Technical Criteria for the Coordination between Power Supply and Rolling Stock to Achieve Interoperability*, 2012.

[6] H. Wang, M. Wu and J. Sun, "Analysis of Low-Frequency Oscillation in Electric Railways Based on Small-Signal Modeling of Vehicle-Grid System in dq Frame," *IEEE Trans. Power Electron.*, vol. 30, no. 9, pp. 5318-5330, Jan. 2015.

[7] Y. Liao, Z. Liu, G. Zhang and C. Xiang, "Vehicle-Grid System Modeling and Stability Analysis With Forbidden Region-Based Criterion," *IEEE Trans. Power Electron.*, vol. 32, no. 5, pp. 3499-3512, May. 2017.

[8] S. Danielsen, O. B. Fosso, M. Molinas, J. A. Suul and T. Toftevaag, "Simplified models of a single-phase power electronic inverter for railway power system stability analysis—Development and evaluation," *Electric Power Systems Research*, vol. 80, no. 2, pp. 204-214, Feb. 2010.

[9] T. Hu, "A Nonlinear-System Approach to Analysis and Design of Power-Electronic Converters With Saturation and Bilinear Terms," *IEEE Trans. Power Electron.*, vol. 26, no. 2, pp. 399-410, Feb. 2011.

[10] Y. Wang, X. Wang, F. Blaabjerg and Z. Chen, "Harmonic Instability Assessment Using State-Space Modeling and Participation Analysis in Inverter-Fed Power Systems," *IEEE Trans. Ind. Electron.*, vol. 64, no. 1, pp. 806-816, Jul. 2016.

[11] X. Wang, F. Blaabjerg and W. Wu, "Modeling and Analysis of Harmonic Stability in an AC Power-Electronics-Based Power System," *IEEE Trans. Power Electron.*, vol. 29, no. 12, pp. 6421-6432, Feb. 2014.

[12] M. Amin and M. Molinas, "Small-Signal Stability Assessment of Power Electronics based Power Systems: A Discussion of Impedance- and Eigenvalue-based Methods," *IEEE Trans. Ind. Appl.*, vol. 53, no. 5, pp. 5014-5030, Sep. 2017.

[13] Z. Shuai, Y. Hu, Y. Peng, C. Tu and Z. J. Shen, "Dynamic Stability Analysis of Synchronverter-dominated Microgrid Based on Bifurcation Theory," *IEEE Trans. on Ind. Electron.*, vol. 64, no. 9, pp. 7467-7477, Sep. 2017.

[14] J. Sun, "Small-Signal Methods for AC Distributed Power Systems–A Review," *IEEE Trans. Power Electron.*, vol. 24, no. 11, pp. 2545-2554, Nov. 2009.

[15] M. Liserre, R. Teodorescu and F. Blaabjerg, "Stability of photovoltaic and wind turbine grid-connected inverters for a large set of grid impedance values," *IEEE Trans. Power Electron.*, vol. 21, no. 1, pp. 263-272, Jan. 2006.

[16] L. Zhang, L. Harnefors and H. P. Nee, "Modeling and Control of VSC-HVDC Links Connected to Island Systems," *IEEE Trans. Power Syst.*, vol. 26, no. 2, pp. 783-793, May. 2011.

[17] T. Dragičević, X. Lu, J. C. Vasquez and J. M. Guerrero, "DC Microgrids—Part I: A Review of Control Strategies and Stabilization Techniques," *IEEE Trans. Power Electron.*, vol. 31, no. 7, pp. 4876-4891, Jul. 2016.

[18] F. Gao, S. Bozhko, A. Costabeber, G. M. Asher and P. W. Wheeler, "Control Design and Voltage Stability Analysis of a Droop-Controlled Electrical Power System for More Electric Aircraft," *IEEE Trans. Ind. Electron.*, vol. 64, no. 12, pp. 9271-9281, Dec. 2017.

[19] R. D. Middlebrook, " Input Filter Considerations in Design and Application of Switching Regulators," *Rec. IEEE Ind. Appl. Soc. Annu. Meeting*, pp. 366-382, 1976.

[20] L. Harnefors, "Proof and Application of the Positive-Net-Damping Stability Criterion," *IEEE Trans. Power Syst.*, vol. 26, no. 1, pp. 481-482, Feb. 2011.

[21] L. Harnefors, M. Bongiorno and S. Lundberg, "Input-Admittance Calculation and Shaping for Controlled Voltage-Source Converters," *IEEE Trans. Ind. Electron.*, vol. 54, no. 6, pp. 3323-3334, Dec. 2007.

[22] S. Vesti, T. Suntio, J. A. Oliver and R. Prieto, "Impedance-Based Stability and Transient-Performance Assessment Applying Maximum Peak Criteria," *IEEE Trans. Power Electron.*, vol. 28, no. 5, pp. 2099-2104, May. 2013.

[23] B. Wen, D. Boroyevich, R. Burgos and P. Mattavelli, "Analysis of D-Q Small-Signal Impedance of Grid-Tied Inverters," *IEEE Trans. Power Electron.*, vol. 31, no. 1, pp. 675-687, Jan. 2016.

[24] H. Hu, H. Tao, F. Blaabjerg, X. Wang, Z. He and S. Gao, "Train-Network Interactions and Stability Evaluation in High-Speed Railways--Part I: Phenomena and Modeling," *IEEE Trans. Power Electron.*, to be published, DOI: 10.1109/TPEL.2017.2781880.

[25] X. Wang, L. Harnefors and F. Blaabjerg, "Unified Impedance Model of Grid-Connected Voltage-Source Converters," *IEEE Trans. Power Electron.*, vol. 33, no. 2, pp. 1775-1787, Feb. 2018.
[26] H. Lee, C. Lee, G. Jang and S. H. Kwon, "Harmonic analysis of the korean high-speed railway using the eight-port representation model," *IEEE Trans. Power Del.*, vol. 21, no. 2, pp. 979-986, Mar. 2006.
[27] B. Lutrakulwattana, M. Konghirun and A. Sangswang, " Harmonic resonance assessment of 1×25kV, 50Hz traction power supply system for suvarnabhumi airport rail link," *Proc. IEEE Int. Electrical Mach. and Syst. Conf.*, pp. 752-755, 2016.
[28] M. Brenna, F. Foiadelli and D. Zaninelli, "Electromagnetic Model of High Speed Railway Lines for Power Quality Studies," *IEEE Trans. Power Syst.*, vol. 25, no. 3, pp. 1301-1308, Aug. 2010.
[29] A. Mariscotti, P. Pozzobon and M. Vanti, "Simplified Modeling of 2×25 kV AT Railway System for the Solution of Low Frequency and Large-Scale Problems," *IEEE Trans. Power Del.*, vol. 22, no. 1, pp. 296-301, Jan. 2007.
[30] Z. He, H. Hu, Y. Zhang and S. Gao, "Harmonic Resonance Assessment to Traction Power-Supply System Considering Train Model in China High-Speed Railway," *IEEE Trans. Power Del.*, vol. 29, no. 4, pp. 1735-1743, Oct. 2014.
[31] H. Hu, S. Gao, Y. Shao, K. Wang, Z. He and L. Chen, "Harmonic Resonance Evaluation for Hub Traction Substation Consisting of Multiple High-speed Railways," *IEEE Trans. on Power Del.*, vol. 32, no. 2, pp. 910-920, Apr. 2017.
[32] H. Hu, Z. He, X. Li, K. Wang and S. Gao, "Power-Quality Impact Assessment for High-Speed Railway Associated With High-Speed Trains Using Train Timetable–Part I: Methodology and Modeling," *IEEE Trans. on Power Del.*, vol. 31, no. 2, pp. 693-703, Aug. 2016.
[33] F. Mahdavizadeh, "Resonance verification of Tehran-Karaj electrical railway," *Proc. 1st Power Qual. Conf., Tehran*, pp. 1-6, 2010.
[34] R. E. Morrison and J. C. W. Corcoran, "Specification of an overvoltage damping filter for the National Railways of Zimbabwe," *IEE Proc. B - Electric Power Appl.*, vol. 136, no. 6, pp. 249-256, 1989.
[35] Z. He, Z. Zheng and H. Hu, "Power quality in high-speed railway systems," *International Journal of Rail Transportation*, vol. 4, no. 2, pp. 71-97, Feb. 2016.
[36] M. B. J. L. J. Agorreta, "Modeling and control of N-paralleled grid-connected inverters with LCL filters coupled due to grid impedance in PV plants," *IEEE Trans. Power Electron.*, vol. 26, no. 3, pp. 770-785, Mar. 2011.
[37] B. Anderson and M. Gevers, "On multivariable pole- zero cancellations and the stability of feedback systems," *IEEE Trans. on Circuits Syst.*, vol. 28, no. 8, pp. 830-833, Aug. 1981.
[38] Y. Li, Q. Liu, S. Hu, F. Liu, Y. Cao, L. Luo and C. Rehtanz, "A Virtual Impedance Comprehensive Control Strategy for the Controllably Inductive Power Filtering System," *IEEE Trans. on Power Electron.*, vol. 32, no. 2, pp. 920-926, Feb. 2017.

Haidong Tao (S'17), received the B.S. degree in electrical engineering from Southwest Jiaotong University, China, in 2015. He is currently pursuing the Ph.D. degree in electrical engineering at Southwest Jiaotong University.

His research interests include modeling and control of high-speed trains and grid-connected converters, harmonics analysis and control, stability of power electronic based power systems.

Haitao Hu (S'13-M'14), received the B.S. degree from Zhengzhou University, Zhengzhou, China, in 2010, and the Ph.D. degree from Southwest Jiaotong University, Chengdu, China, in 2014, all in electrical engineering. From 2013 to 2014, He worked as a visiting doctoral scholar at University of Alberta, Edmonton, Canada. Currently, he is an Associate Professor with School of electrical engineering at Southwest Jiaotong University.

His main research interests are power quality and stability of the electric traction system.

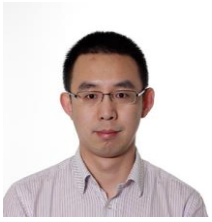

Xiongfei Wang (S'10-M'13-SM'17) received the B.S. degree from Yanshan University, Qinhuangdao, China, in 2006, the M.S. degree from Harbin Institute of Technology, Harbin, China, in 2008, both in electrical engineering, and the Ph.D. degree in energy technology from Aalborg University, Aalborg, Denmark, in 2013. Since 2009, he has been with the Aalborg University, Aalborg, Denmark, where he is currently an Associate Professor in the Department of Energy Technology. His research interests include modeling and control of grid-connected converters, harmonics analysis and control, passive and active filters, stability of power electronic based power systems.

Dr. Wang serves as an Associate Editor for the IEEE Transactions on Power Electronics, the IEEE Transactions on Industry Applications, and the IEEE Journal of Emerging and Selected Topics in Power Electronics. He is also the Guest Editor for the Special Issue "Grid-Connected Power Electronics Systems: Stability, Power Quality, and Protection" in the IEEE Transactions on Industry Applications. He received the second prize paper award and the outstanding reviewer award of IEEE Transactions on Power Electronics in 2014 and 2017, respectively, the second prize paper award of IEEE Transactions on Industry Applications in 2017, and the best paper awards at IEEE PEDG 2016 and IEEE PES GM 2017.

Frede Blaabjerg (S'86–M'88–SM'97–F'03) was with ABB-Scandia, Randers, Denmark, from 1987 to 1988. From 1988 to 1992, he got the PhD degree in Electrical Engineering at Aalborg University in 1995. He became an Assistant Professor in 1992, an Associate Professor in 1996, and a Full Professor of power electronics and drives in 1998. From 2017 he became a Villum Investigator.

His current research interests include power electronics and its applications such as in wind turbines, PV systems, reliability, harmonics and adjustable speed drives. He has published more than 500 journal papers in the fields of power electronics and its applications. He is the co-author of two monographs and editor of 6 books in power electronics and its applications.

He has received 24 IEEE Prize Paper Awards, the IEEE PELS Distinguished Service Award in 2009, the EPE-PEMC Council Award in 2010, the IEEE William E. Newell Power Electronics Award 2014 and the Villum Kann Rasmussen Research Award 2014. He was the Editor-in-Chief of the IEEE Transactions on Power Electronics from 2006 to 2012. He has been Distinguished Lecturer for the IEEE Power Electronics Society from 2005 to 2007 and for the IEEE Industry Applications Society from 2010 to 2011 as well as 2017 to 2018.

He is nominated in 2014, 2015, 2016 and 2017 by Thomson Reuters to be between the most 250 cited researchers in Engineering in the world. In 2017 he became Honoris Causa at University Politehnica Timisoara (UPT), Romania.

Zhengyou He (M'10-SM'13), received the B.Sc. degree and M. Sc. degree in Computational Mechanics from Chongqing University, Chongqing, China, in 1992 and 1995, respectively. He received the Ph.D. degree in the School of Electrical Engineering from Southwest Jiaotong University, Chengdu, China, in 2001. Currently, he is a Professor in the School of Electrical Engineering at Southwest Jiaotong University.

His research interests include signal process and information theory applied to electrical power system, and application of wavelet transforms in power system.